Mon. Not. R. Astron. Soc. **372,** 923–932 (2006) doi:10.1111/j.1365-2966.2006.10900.x

A multidimensional, adiabatic hydrodynamics code for studying tidal excitation

Avery E. Broderick[1⋆] and Yasser Rathore[2⋆]

[1]*Institute for Theory and Computation, Harvard-Smithsonian Center for Astrophysics, 60 Garden St., MS 51 Cambridge, MA 02138, USA*
[2]*Theoretical Astrophysics, Caltech, 130-33 Pasadena, CA 91125, USA*

Accepted 2006 August 3. Received 2006 July 21; in original form 2006 May 16

ABSTRACT

We have developed a massively parallel, simple and fast hydrodynamics code for multidimensional, self-gravitating and adiabatic flows. Our primary motivation is the study of the non-linear development of white dwarf oscillations excited via tidal resonances, typically over hundreds of stellar dynamical times. Consequently, we require long-term stability, low diffusivity and high-numerical efficiency. This is accomplished by an Eulerian finite-difference scheme on a regular Cartesian grid. This choice of coordinates provides uniform resolution throughout the flow as well as simplifying the computation of the self-gravitational potential, which is done via spectral methods. In this paper, we describe the numerical scheme and present the results of some common diagnostic problems. We also demonstrate the stability of a cold white dwarf in three dimensions over hundreds of dynamical times. Finally, we compare the results of the numerical scheme to the linear theory of adiabatic oscillations, finding numerical quality factors on the order of 6000 and excellent agreement with the oscillation frequency obtained by the linear analysis.

Key words: hydrodynamics – methods: numerical – binaries: close – white dwarfs.

1 INTRODUCTION

White dwarfs (WDs) are known to be common endpoints of stellar evolution. A significant amount of evidence suggests that both stellar mass black holes ($< 10^2\,M_\odot$) and neutron stars are also relatively common. More recently, both theoretical (see e.g. Madau & Rees 2001) and the observational (see e.g. Colbert & Ptak 2002; Gerssen et al. 2002) studies have implied the existence of intermediate mass black holes (10^2–$10^5\,M_\odot$). As a result, it appears inevitable that WD–compact object binaries will form. This may be especially likely within globular clusters.

The subsequent evolution of a WD–compact object binary will typically be driven by gravitational radiation. As the system passes through resonances between the oscillation frequencies of the WD and the orbit, it is possible to resonantly excite oscillation modes on the WD. Even small amounts of energy transfer may have an impact upon the orbit, having implications for Laser Interferometer Space Antenna (LISA). Large energy transfers may result in the detonation of the WD, leading to an abnormal Type Ia supernova and perhaps a subsequent γ-ray burst. In order to address the magnitude and likelihood of either of these outcomes it is necessary to understand the mode excitation process in detail. For the linear regime this has been done (see Rathore, Broderick & Blandford 2003). In Rathore, Blandford & Broderick (2005) it was found that it was frequently possible to excite modes to non-linear amplitudes in these systems. Therefore, it is now necessary to investigate the non-linear mode evolution. This is most directly done using numerical hydrodynamics simulations.

A number of hydrodynamics codes, which may be used for this purpose currently exist. Two such codes, ZEUS (Stone & Norman 1992) and FLASH (Fryxell et al. 2000) have been developed to be generic hydrodynamic engines. This has the advantage of providing access to a sophisticated suite of hydrodynamic simulation tools. However, it also has the disadvantage of being complicated to use and perhaps suboptimal for our specific problem. In addition, to a good approximation the WD oscillations are adiabatic, and hence detailed treatment of shocks and entropy generation are unnecessary.

Motl, Tohline & Frank (2002) have developed an adiabatic hydrodynamics code, primarily to study binary mass transfer. However, the choice of cylindrical coordinates, while useful in the binary transfer application, also presents problems when applied to an oscillating WD. In the later case it is important to maintain uniform resolution throughout the star. Furthermore, a cylindrical coordinate system complicates the advection scheme. These difficulties are trivially removed in Cartesian coordinates, an additional advantage of which is the ease of application of a spectral Poisson equation solver.

We present a simple hydrodynamics code with some common diagnostics and an example application. This is done in seven sections with Section 2 reviewing the hydrodynamic equations, Section 3 outlining the differencing scheme used, Section 4 describing

⋆E-mail: abroderick@cfa.harvard.edu (AEB); yasser.rathore@gmail.com (YR)

the method used to solve the Poisson equation, Section 5 presenting some tests of the code, Section 6 applying the code to an oscillating WD and Section 7 containing concluding remarks.

2 GOVERNING HYDRODYNAMIC EQUATIONS

There is considerable freedom in the choice of macroscopic quantities used to describe fluid flows. Our choice was motivated by the numerical convenience of the flux-conservative form the hydrodynamic equations. Unfortunately, since we will ultimately be interested in tidally exciting oscillations, we leave open the possibility of an external force term that cannot be expressed in the form of a gradient. Therefore, we employ a 'sourced advective form' of the hydrodynamic equations, for which the advection steps are still strictly conservative. In addition, since we are restricting ourselves to adiabatic flows, it is convenient to use the entropy rather than the energy as a thermodynamic variable. We therefore describe the fluid flow by its mass density (ρ), entropy density (s) and momentum density ($\boldsymbol{J}$).

The equations for ρ and s have a purely advective form,

$$\frac{\partial \rho}{\partial t} + \boldsymbol{\nabla} \cdot \boldsymbol{v}\rho = 0 \tag{1}$$

$$\frac{\partial s}{\partial t} + \boldsymbol{\nabla} \cdot \boldsymbol{v}s = 0, \tag{2}$$

which corresponds to the conservation of mass and entropy.[1] The equation for $\boldsymbol{J}$ can be written in a sourced advective form,

$$\frac{\partial \boldsymbol{J}}{\partial t} + \boldsymbol{\nabla} \cdot \boldsymbol{v}\boldsymbol{J} = -\boldsymbol{\nabla} P - \rho \boldsymbol{\nabla} \Phi + \boldsymbol{f}, \tag{3}$$

where the pressure (P) is given by an equation of state,

$$P = P(\rho, s), \tag{4}$$

the self-gravitational potential (Φ) is determined by the Poisson equation,

$$\nabla^2 \Phi = 4\pi G \rho, \tag{5}$$

and $\boldsymbol{f}$ is any additional external force per unit volume acting on the fluid (e.g. in the case of a compact binary, tidal and/or Coriolis forces).

3 DIFFERENCING SCHEME

In one dimension, a staggered mesh avoids interpolating the flow velocities to the cell boundaries. However, in many dimensions, the interpolation of vector quantities (e.g. momentum) cannot be avoided and thus complicates the advection steps in the momentum conservation equation (3). Therefore, we use a zone-centred, uniform Cartesian grid.

Casting the hydrodynamic equations in a sourced advective form allows the explicit conservation of mass and entropy, and momentum when in hydrodynamic equilibrium.

[1] Note that s is the entropy per unit volume and not the specific entropy. Hence, in our notation, the adiabatic condition is

$$\frac{\mathrm{d}}{\mathrm{d}t}\left(\frac{s}{\rho}\right) = 0\,,$$

where $\mathrm{d}/\mathrm{d}t$ is the convective derivative.

3.1 Advection

The advection steps in equations (1)–(3) may be integrated to yield finite-volume equations for a given cell

$$\Delta\lambda = \frac{\Delta t}{\Delta V} \sum_{i=x,y,z} \left(\Lambda_{-i} - \Lambda_{+i}\right) \Delta S_i, \tag{6}$$

where $\Delta\lambda$ is the change in the quantity λ due to fluid advection, Δt is the time-step, ΔV is the cell volume, $\Lambda_{\pm i}$ are the fluxes of the quantity λ at the $\pm$ ith boundary of the cell, and ΔS_i is the area of the cell surface normal to the ith direction.

In general some interpolation method is required to determine the values of the fluxes at the boundaries of the cell. We broke the interpolation of the fluxes into an interpolation over the fluid velocity and an interpolation over the advected quantities,

$$\Lambda_{\pm i} = \lambda^*_{\pm i} \overline{v}_{\pm i}, \tag{7}$$

where $\overline{v}_{\pm i}$ is the interpolated component of the velocity normal to the $\pm i$th cell face at the cell boundary, and λ^* is the interpolated value of the advected quantity. The $\overline{v}_{\pm i}$ is defined by

$$\overline{v}_{\pm i} = \frac{J^i + J^i_{\pm i}}{\rho + \rho_{\pm i}}, \tag{8}$$

which ensures that it is not divergent in low-density cells.

A numerical difficulty with the interpolation of the advected quantities is that advecting the volumetric densities tends to generate unphysically high velocities in low-mass density cells. We circumvented this problem by using consistent transport (Stone & Norman 1992), in which it is the specific quantities that are interpolated, i.e.

$$\lambda^*_{\pm i} = \overline{\rho}_{\pm i} (\overline{\lambda/\rho})_{\pm i}, \tag{9}$$

where $\overline{\rho}_{\pm i}$ and $(\overline{\lambda/\rho})_{\pm i}$ are the interpolated values of ρ and the specific quantity λ/ρ at the $\pm i$th boundary of the cell.

The advection scheme is inherently unstable. This may be addressed in a variety of ways (e.g. Gudonov schemes, Lax–Wendroff, Leap-frog, upwinding, etc.). However, since we do not anticipate strong shocks in our primary application, upwinding schemes provide an economical solution. We implement three such schemes, differing in the order of interpolation: donor cell (zero order), van Leer (first order) and piecewise parabolic advection (PPA, second order).

3.1.1 Donor cell upwinding

The donor cell method is a first-order upwinding scheme, approximating the spatial distribution of a given quantity, q, as a step function. In this method all information from the downwind cell is ignored, that is, at the $-$ ith cell boundary

$$\overline{q}_{-i} = \begin{cases} q_{-i} & \text{if} \quad \overline{v}_{-i} \geqslant 0 \\ q & \text{if} \quad \overline{v}_{-i} < 0 \end{cases}. \tag{10}$$

For a given cell, this only requires information from the nearest neighbours. In practice, donor cell upwinding is highly diffusive (see e.g. Section 5.1), and hence was not used beyond the testing stage.

3.1.2 van Leer upwinding

The van Leer upwinding method is a second-order method first described by its namesake (van Leer 1977a,b, 1979). In contrast to the donor cell, the distribution of q is approximated by a piecewise linear function. The slopes of these linear functions are given by the

so-called van Leer slopes, defined below for a given cell along the ith direction,

$$\mathrm{d}q_i = \begin{cases} \dfrac{2(q_{+i}-q)(q-q_{-i})}{\Delta x^i (q_{+i}-q_{-i})} & \text{if} \quad (q_{+i}-q)(q-q_{-i}) > 0 \\ 0 & \text{otherwise} \end{cases}. \quad (11)$$

In terms of the van Leer slopes, the upwinded value of the quantity q at the $-i$th cell boundary is given by

$$\overline{q}_{-i} = \begin{cases} q_{-i} + \frac{1}{2}\left(\Delta x^i - \overline{v}_{-i}\Delta t\right)\,\mathrm{d}q_{-i,i} & \text{if} \quad \overline{v}_{-i} \geqslant 0 \\ q - \frac{1}{2}\left(\Delta x^i + \overline{v}_{-i}\Delta t\right)\,\mathrm{d}q_i & \text{if} \quad \overline{v}_{-i} < 0 \end{cases}. \quad (12)$$

Near local maxima, van Leer reverts to zero order (donor cell) and thus becomes highly diffusive, resulting in the stabilization of the differencing scheme. Because van Leer upwinding employs the van Leer slopes of neighbouring cells, it requires information from both the nearest and the next nearest neighbours.

3.1.3 *PPA upwinding*

The PPA method is a third-order method originally developed by Colella & Woodward (1984). It approximates the distribution of q by a piecewise parabolic function. The essence of the method is the determination of the monotonized left and right interface values, q_{L} and q_{R}, which are computed via equations (1.6)–(1.10) in Colella & Woodward (1984). In terms of q_{L} and q_{R}, the upwinded value of q at the $-i$th cell boundary is given by

$$\overline{q}_{-i} = \begin{cases} q_{\mathrm{R},-i} + \xi(q_{-i} - q_{\mathrm{R},-i}) & \\ \quad +\xi(1-\xi)(2q_{-i} - q_{\mathrm{R},-i} - q_{\mathrm{L},-i}) & \text{if} \quad \overline{v}_{-i} \geqslant 0 \\ q_L + \xi(q - q_{\mathrm{L}}) & \\ \quad +\xi(1-\xi)(2q - q_{\mathrm{R}} - q_{\mathrm{L}}) & \text{if} \quad \overline{v}_{-i} < 0 \end{cases}, \quad (13)$$

where $\xi = \overline{v}_{-i}\Delta t/\Delta x^i$.

The PPA method is substantially less diffusive than the van Leer method. This is especially notable at discontinuities, where the profiles generated by PPA are significantly steeper than those generated by the van Leer scheme. However, the improvement comes with a relatively high computational cost. It has been found by Stone & Norman (1992) that, typically, increasing the grid resolution is a computationally more efficient way to obtain greater accuracy. For this reason, unless explicitly stated otherwise, we have used the van Leer upwinding method.

3.2 Artificial viscosity

In the context of numerical Eulerian upwinding schemes, shocks can lead to unphysical results, and in this case, uphysical oscillations near discontinuities. If resolving the shock is critical, this may be cured via the introduction of Riemann solvers (capable of localizing the shock to a single cell boundary). However, if resolving the shock is unnecessary, it is significantly easier to introduce an artificial numerical viscosity. While several prescriptions for implementing numerical viscosity can be found in the literature, we chose to implement the von Neumann–Richtmyer scheme due to its ability to produce the correct shock propagation velocity and its low diffusivity far from the shock (a direct result of the fact that it is introduced only in regions of strong compression Stone & Norman 1992). This approach takes the form of defining a viscous pseudo-pressure for each direction which is non-vanishing in regions of compression only:

$$Q^i = \begin{cases} l^2\rho\left(\dfrac{\partial v^i}{\partial x^i}\right)^2 & \text{if} \quad \dfrac{\partial v^i}{\partial x^i} < 0 \\ 0 & \text{otherwise} \end{cases}, \quad (14)$$

for $i = x, y, z$, where l is the length-scale over which the shocks are to be smoothed. The associated source term to equation (3) is given by

$$F^i_{\mathrm{visc}} = -\frac{\partial Q^i}{\partial x^i}. \quad (15)$$

Typically this will smooth the shock front over a number of cells, a distance that is usually much larger than the natural shock depth.

It should also be noted that a correct treatment of shocks is precluded by the adiabatic condition, equation (2). This can be remedied by the inclusion of a viscous source term in the entropy equation. However, since for the applications we envision shocks will result in the rapid thermalization of the bulk kinetic energy of the stellar oscillations, their mere production may make a purely hydrodynamic description inapplicable. In particular, thermonuclear processes could dominate at this point, and thus neither the added complexity and computational overhead of the Reimann solver methods nor the complication of an entropy source term are required.

3.3 Momentum source terms

In addition to advection, the momentum density evolves due to pressure gradients and gravitational interactions. We found that simply finite-differencing ∇P leads to a significantly less stable system than calculating the gradient via analytical partial derivatives and finite-differences in ρ and s. In contrast, the gravitational acceleration was obtained directly in terms of a second order, finite-difference of the gravitational potential (the details of solving for which are presented in Section 4).

The finite differencing of the viscous force is performed in two steps (i) determining the viscous pseudo-pressure and (ii) finite differencing the viscous pseudo-pressure to obtain the viscous force directly. In finite difference form, the viscous pseudo-pressure is defined by

$$Q^i_{\pm i} = \begin{cases} \eta\dfrac{\rho_{\pm i}+\rho}{2}\left(\dfrac{v^i_{\pm i} - v^i}{\Delta x^i}\right)^2 & \text{if} \quad \pm\left(v^i_{\pm i} - v^i\right) < 0 \\ 0 & \text{otherwise} \end{cases}, \quad (16)$$

for $i = x, y, z$. The dimensionless coefficient η is approximately the number of cells to smooth discontinuities over. We have typically used $\eta = 2$. The viscous force is then determined by

$$F^i_{\mathrm{visc}} = -\frac{Q^i_{+i} - Q^i_{-i}}{\Delta x^i}. \quad (17)$$

Therefore, excluding external forces, the source terms in equation (3) are given by

$$-\left(\frac{\partial P}{\partial \rho}\right)_s \frac{\rho_{+i} - \rho_{-i}}{2\Delta x^i} \qquad -\left(\frac{\partial P}{\partial s}\right)_\rho \frac{s_{+i} - s_{-i}}{2\Delta x^i}$$
$$-\rho\frac{\Phi_{+i} - \Phi_{-i}}{2\Delta x^i} + F^i_{\mathrm{visc}}, \quad (18)$$

for $i = x, y, z$.

When using a barotropic equation of state, $P(\rho)$, it can be convenient to write the source terms in terms of the specific enthalpy, h,

$$-\rho\left(\frac{h_{+i} - h_{-i}}{2\Delta x^i} + \frac{\Phi_{+i} - \Phi_{-i}}{2\Delta x^i}\right) + F^i_{\mathrm{visc}}, \quad (19)$$

for $i = x, y, z$. An example of when this may be useful will be discussed in Section 6. Note that in this case, the entropy equation is superfluous.

3.4 Courant–Friedrichs–Lewy time-step

The stability of the finite-difference scheme requires that the time-step obey the Courant–Friedrichs–Lewy (CFL) criterion. This reduces to the physical consideration that for the evolution of a given cell to be dependent upon quantities only in that cell, the time-step must be sufficiently small that information cannot propagate into it from neighbouring cells. That is,

$$\Delta t \leqslant t_{\rm CFL}, \tag{20}$$

where the CFL time is defined by

$$t_{\rm CFL} = \min\left(\frac{\Delta x}{c_s + |v^x|}, \frac{\Delta y}{c_s + |v^y|}, \frac{\Delta z}{c_s + |v^z|}\right), \tag{21}$$

where c_s is the local adiabatic sound speed (see e.g. Motl et al. 2002; Stone & Norman 1992, and references therein). In addition, the inclusion of an artificial viscosity imposes the additional requirement that the time-step does not exceed the time-scale for diffusion across cell width length-scales:

$$t_{\rm visc} = \min\left(\frac{\Delta x}{4\eta|\Delta v^x|}, \frac{\Delta y}{4\eta|\Delta v^y|}, \frac{\Delta z}{4\eta|\Delta v^z|}\right) \tag{22}$$

(see e.g. Stone & Norman 1992). In practice, for many operator split methods taking the time-step to be the CFL time does not ensure stability, rather it is necessary to take Δt to be some fraction of $t_{\rm CFL}$ or $t_{\rm visc}$. We have found that a robust choice for the Courant number to be 0.25, i.e.

$$\Delta t \leqslant \frac{1}{4}\min(t_{\rm CFL}, t_{\rm visc}). \tag{23}$$

From equation (21) it is clear that the cells with the highest velocities (both kinetic and sound) will provide the most stringent limits on the time-step. Examples are the cells constituting the accreting vacuum surrounding the star. In practice, no portion of the grid can have vanishing density for numerical reasons. Therefore 'zero' density was taken to be 10^{-8} of the initial maximum density. As a result, the vacuum is physically insignificant. Nevertheless, because of their large velocities (though negligible momentum densities), these cells can be the limiting factor in determining the time-step. In order to rectify this problem we impose a velocity cap. The CFL time is set by considering only cells with densities larger than 10^{-6} of the maximum density. The remaining cells have their velocities capped at

$$v_{\rm cap} = \min\left(\frac{\Delta x}{\Delta t}, \frac{\Delta y}{\Delta t}, \frac{\Delta z}{\Delta t}\right), \tag{24}$$

so as not to drive the time-step down. While this explicitly violates the hydrodynamic equations presented in Section 2 (effectively making the vacuum extremely viscous), it does so in a physically negligible manner in the current context.

We operator split the source and advection contributions to the evolution of the fluid quantities at each time-step. Despite this, we do not make use of dimensional operator splitting, making this a variation of the unsplit method of van Leer. Therefore, a single time-step is taken in three stages (1) taking half of the source step, (2) performing the updates due to advection and (3) taking the second half of the source step. The gravitational potential is recalculated at each source step.

3.5 Boundary conditions

Because the upwinding methods require information about neighbouring cells, it is necessary to provide a boundary of ghost cells along the outer edges of the grid. As these ghost cells are not evolved themselves, they require some prescription for assigning the evolved quantities to them. We considered three types of boundary conditions: fixed, replicated and outflow.

The first, and the simplest, is the fixed boundary condition. In this prescription, the boundary cells are fixed to have 'zero' density, entropy density and momentum flux. This tends to limit the velocity of the 'zero' density vacuum by not providing a boundary momentum flux.

The second set of boundary conditions consists of replicating the last set of cells in the grid. This provides a slightly more realistic set of boundary conditions, allowing the accretion of the 'zero' density vacuum to stabilize through hydrodynamic balance. If a physically significant portion of the flow is crossing the boundary this is significantly superior to the first scheme.

The third set of boundary conditions employed were the so-called outflow boundary conditions. In this prescription, fluid is allowed to flow off of the grid but not return. In order to prevent the boundaries from physically affecting the fluid on the grid, the boundary values for density and entropy are chosen to preserve hydrostatic equilibrium in the last grid zone. Note that this does not stop the fluid from advecting off of the grid through this zone. As a result, this minimizes the creation of spurious reflections at the boundaries. For a self-gravitating fluid that is initially entirely contained within the grid, this provides the most realistic set of conditions.

3.6 Parallelization

The primary purpose for the development of our code is to perform high-resolution studies of the non-linear evolution of normal modes in WDs. The resulting computational requirements necessitate high-performance computing. Because the sourced advection step for a given cell depends only upon cells in its immediate neighbourhood, it naturally lends itself to a straightforward parallelization scheme. This takes the form of dividing the entire grid into a number of subdomains, each of which are handled by a separate processor. Because interprocessor communication incurs substantial performance penalties, we choose a domain decomposition that minimizes the communication required. The source of interprocessor communication in each sourced advection step is the need for neighbour data around the edges of each subdomain. Therefore, the time-penalties due to interprocessor communication are dictated by the surface area of each subdomain, as well as the depth of neighbours that is necessary (one for the donor cell, two for the van Leer and three for the PPA upwinding schemes). Hence, minimizing the surface area of the subdomains minimizes the interprocessor communication.

We have implemented our code in the C++ programming language. This choice was motivated by considerations such as modularity of design, flexibility, efficiency, ease of code reuse and extensibility. For example, the object-oriented structure of the C++ language has allowed us to maintain a clean separation between interfaces and implementations (e.g. for the equation of state, Poisson equation solver, initial conditions, etc.), and features such as templates have allowed us to write generic code without sacrificing runtime performance.

Since standard C++ does not provide facilities for parallel computing, it was necessary to use additional libraries for this purpose.

parallelization. We have implemented parallelization via the message passing interface (MPI). Since both optimizing ISO-compliant C++ compilers and high-quality MPI implementations are available for virtually every major computing platform, our code is highly portable.

4 SOLVING THE POISSON EQUATION

Equation (5) differs from the other governing equations in that it is not evolutionary, that is, it must be solved over the entire grid at each time-step. A number of methods for solving the Poisson equation have been presented in the literature, including general elliptical equation solvers, multigrid methods, multipole methods and spectral methods. Of these, due to the efficiency of the fast-Fourier transform algorithm, spectral methods tend to be the most efficient, and implementing them on a fixed Cartesian grid is straightforward.

The solution of the Poisson equation requires the specification of boundary conditions on some closed surface. In most physical problems, this surface is chosen to lie at infinity, upon which the potential is chosen to vanish. However, since our computational domain is finite, it is not possible to impose boundary conditions at infinity in a straightforward manner. Instead, we define the value of the potential on the surface of our domain, which we compute via a multipole expansion:

$$\Phi^B(\boldsymbol{x}) = -\sum_{l=0}^{\infty}\sum_{m=-l}^{l}\frac{4\pi G}{2l+1}r^{-l-1}Q_{lm}Y_{lm}(\hat{\boldsymbol{x}}), \tag{25}$$

where

$$Q_{lm} = \int \mathrm{d}\boldsymbol{x}' r'^{l} Y^*_{lm}(\hat{\boldsymbol{x}}')\rho(\boldsymbol{x}'). \tag{26}$$

In practice, it is only necessary to include the first few multipoles (for our purposes $l_{\max} = 5$) to obtain accurate boundary conditions.

Given the Dirichlet boundary conditions, it is possible to solve Poisson equation via a discrete sine transform (DST; see, e.g. Press et al. 1992). Written in its finite-difference form, (5) becomes

$$\sum_{i=x,y,z}\frac{\Phi_{+i}-2\Phi+\Phi_{-i}}{(\Delta x^i)^2} = 4\pi G\rho. \tag{27}$$

In terms of their DSTs $\widehat{\Phi}$ and $\widehat{\rho}$, Φ and ρ are given by

$$\Phi_{i,j,k} = \frac{2}{IJK}\sum_{m=1}^{I-1}\sum_{n=1}^{J-1}\sum_{p=1}^{K-1}\widehat{\Phi}_{m,n,p}\sin\frac{\pi im}{I}\sin\frac{\pi jn}{J}\sin\frac{\pi kp}{K} \tag{28}$$

$$\rho_{i,j,k} = \frac{2}{IJK}\sum_{m=1}^{I-1}\sum_{n=1}^{J-1}\sum_{p=1}^{K-1}\widehat{\rho}_{m,n,p}\sin\frac{\pi im}{I}\sin\frac{\pi jn}{J}\sin\frac{\pi kp}{K}, \tag{29}$$

where i,j,k and I,J,K define the location on, and the dimensions of, the computational domain, respectively. Substituting these expansions into (27) gives

$$\widehat{\Phi}_{m,n,p} = -4\pi G\frac{\widehat{\rho}_{m,n,p}}{\kappa^2_{m,n,p}}, \tag{30}$$

where

$$\kappa^2_{m,n,p} = \frac{2}{(\Delta x)^2}\left(1-\cos\frac{\pi m}{I}\right) + \frac{2}{(\Delta y)^2}\left(1-\cos\frac{\pi n}{J}\right) + \frac{2}{(\Delta z)^2}\left(1-\cos\frac{\pi p}{K}\right).$$

The potential $\Phi_{i,j,k}$ is then computed from (28).

Expanding Φ in terms of the sine basis functions of the Fourier series ensures that it vanishes at the boundaries of the domain. Non-zero boundary conditions can be incorporated by adding an appropriate source term to the right side of equation (27). We may define $\Phi' = \Phi - \Phi^B$ where now Φ^B is determined by equation (25) at one zone beyond the boundary and vanishes everywhere else. The resulting equation for Φ' is the same as equation (27) in the interior and is given by

$$\sum_{i=x,y,z}\frac{\Phi'_{+i}-2\Phi'+\Phi'_{-i}}{(\Delta x^i)^2} = 4\pi G\rho - \frac{\Phi^B_{\pm j}}{(\Delta x^j)^2} = 4\pi G\rho', \tag{31}$$

on the $\pm j$th boundary. As a result, the effective source terms are given by

$$\begin{aligned}4\pi G\rho'_{i,j,k} = {} & 4\pi G\rho_{i,j,k} \\ & - \frac{1}{(\Delta x)^2}\left(\delta_{i,1}\Phi^B_{0,j,k} + \delta_{i,I-1}\Phi^B_{I,j,k}\right) \\ & - \frac{1}{(\Delta y)^2}\left(\delta_{j,1}\Phi^B_{i,0,k} + \delta_{j,J-1}\Phi^B_{i,J,k}\right) \\ & - \frac{1}{(\Delta z)^2}\left(\delta_{k,1}\Phi^B_{i,j,0} + \delta_{k,K-1}\Phi^B_{i,j,K}\right).\end{aligned} \tag{32}$$

To summarize, our procedure for solving the Poisson equation is:

(i) Calculate Φ^B via the multipole expansion (25).
(ii) Calculate the effective source terms for Φ' from (32).
(iii) Perform a DST on the effective source terms.

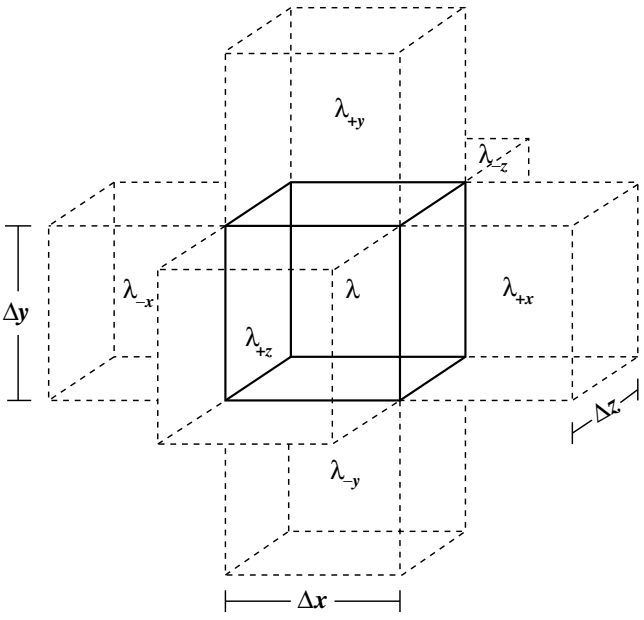

Figure 1. Shown is the geometry of a zone-centred, uniform Cartesian grid, where λ can be any of the five evolved quantities (ρ, s and $\boldsymbol{J}$) or the gravitational potential (Φ).

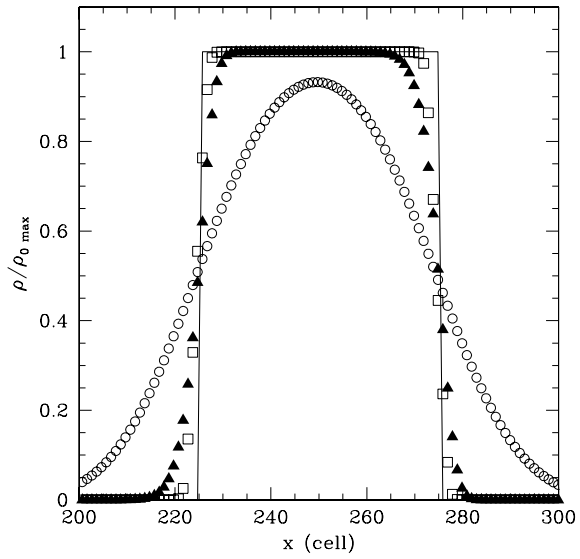

Figure 2. A square pulse that has been advected five times its initial width (50 cells) using the donor cell (open circles), van Leer (filled triangles) and PPA (open squares) upwinding schemes. For reference, the original pulse profile is also shown.

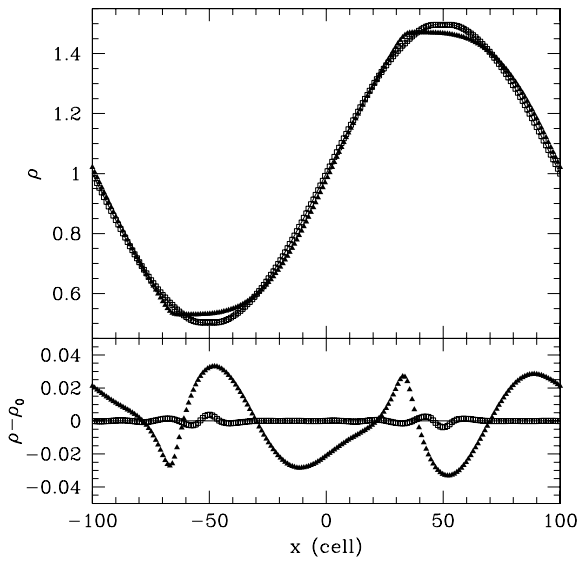

Figure 3. A sine wave is advected with periodic boundary conditions for 100 times its wavelength (200 cells) using the van Leer (filled triangles) and PPA (open squares) upwinding schemes. In the top panel the density profile is shown explicitly, while in the bottom the residuals are plotted. For reference the analytical result is also shown.

(iv) Calculate $\widehat{\Phi}'$ from (30).
(v) Perform a DST on $\widehat{\Phi}'$ to determine Φ'.

We do not actually need to add Φ^B to our final answer since it only affects the ghost points outside our grid. Note that because we use a second-order finite-difference to determine the gravitational acceleration in equation (18) it is necessary to define Φ on an extra surface of ghost cells on each edge of the domain.

The DST is most efficiently parallelized in terms of a slab decomposition of the grid, as opposed to the ideal decomposition for the sourced advection step (which is cubical). As a result, a significant amount of interprocessor communication is required to prepare for the solution of the Poisson equation at each time-step. However, we have found that the time saved by using the DST more than outweighs the penalty incurred by the communication overhead compared to alternative methods (e.g. multigrid and multipolar methods).

5 TEST PROBLEMS

5.1 Advection

In order to test the advection scheme we considered the advection of a square pulse (without source terms). In Fig. 2, the pulse is shown after being advected five times its initial width (50 cells) using both the donor cell and van Leer upwinding methods. It is clear that both methods are diffusive, with the donor cell method substantially more so.

In general diffusion will lead to errors in both the amplitude and the phase of an advected pulse. In order to quantify these errors for diffusion resulting from the upwinding scheme, a sine wave was advected with periodic boundary conditions for 100 times its wavelength. By this time the donor cell upwinding scheme has diffused the sine wave completely, hence only the van Leer and PPA methods are shown in Fig. 3. The errors are at the 4 and 0.4 per cent levels, respectively, with deviations becoming most significant at extrema (where both schemes reduce to zero order). In both the square pulse and the sine wave a noticeable asymmetry (which is determined by the direction of propagation) develops as a result of higher order effects in the upwinding schemes.

5.2 Sod shock tube

The pressure source term in equation (3) was tested by the Sod shock tube problem. The Sod shock tube consists of an initial density and pressure discontinuity and its subsequent evolution for an ideal gas ($\Gamma = 1.4$) and a specific set of initial conditions. For $x > 0$, $\rho = 0.125$ and $P = 0.1$ while for $x \leqslant 0$, $\rho = 1$ and $P = 1$. Because it is the entropy density and not the pressure that is evolved, it is necessary to find s as a function of ρ and P for an ideal gas:

$$s = \ln\left(\frac{P^n}{\rho^{n+1}}\right), \quad \text{where} \quad n = \frac{1}{\Gamma - 1}. \tag{33}$$

The Sod shock tube is useful as a test because the resulting ρ and P profiles for any given time can be calculated analytically. (see e.g. Sod 1978; Hawley, Wilson & Smarr 1984).

In Fig. 4, the numerical results from our code are compared to the analytical solutions. Overall, they are in good agreement, however there are two minor discrepancies. The most notable is the entropy deficit in the post-shock fluid ($0.184 < x < 0.35$). This is a result of using the adiabatic condition instead of energy conservation. In general, entropy is generated at shock fronts, and hence the higher analytical value is easy to understand. Because we intend to apply the code to scenarios in which the adiabatic condition holds to a very good approximation, we expect the entropy deficit to be physically insignificant. The second discrepancy is the overshoots at points where the slopes of quantities change discontinuously. As discussed in Stone & Norman (1992) this is a real result, originating from the numerical viscosity inherent in any finite-difference code. Most importantly, however, is the fact that the artificial viscosity causes the shock fronts to be well behaved in our code.

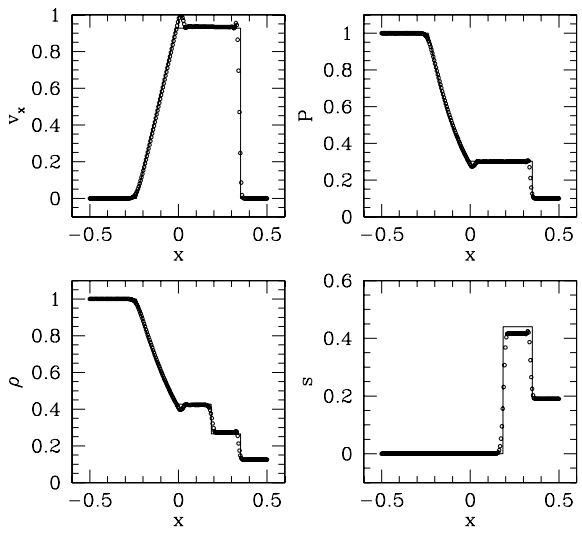

Figure 4. The density, pressure, velocity and entropy are shown for the Sod shock tube at $t = 0.2$ (the units of which depend upon the units chosen for the pressure and density). 200 cells were used with van Leer upwinding. The head and tail of the rarefaction wave are located at $x = -0.235$ and -0.014, respectively. The contact and shock discontinuities are at $x = 0.184$ and 0.35, respectively.

5.3 Pressure-free collapse

The gravitational source term in equation (3) was tested via the pressure-free collapse of a uniform density sphere. Again there is an analytical solution:

$$r = r_0 \cos^2 \beta$$

$$\rho = \rho_0 \cos^{-6} \beta$$

$$t = \left(\beta + \frac{1}{2}\sin 2\beta\right)\left(\frac{8\pi}{3} G\rho_0\right)^{-1/2} \tag{34}$$

(see e.g. Stone & Norman 1992). Fig. 5 depicts the result after allowing the radius to halve (at $t = 0.909$ for $G = 1$), for a $256 \times 256 \times 256$ cell grid. There is a small excess on the edges resulting from our implementations of viscosity and consistent transport (which necessarily treats the advection of velocity into the edges differently due to the density gradients). Overall, it does show good agreement with expectations.

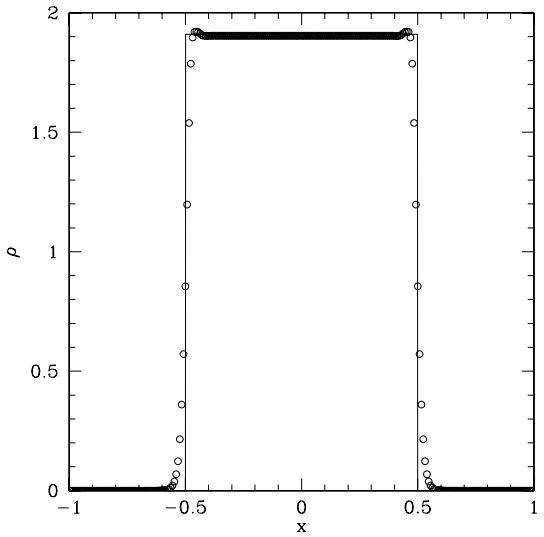

Figure 5. The numerical (open circles) and analytical (solid line) solutions for the density as a function of distance along a radial section for the pressure free collapse of a uniform density sphere are shown. The initial radius and total mass of the sphere was unity. A $256 \times 256 \times 256$ cell grid was used. With Newton's constant given by $G = 1$, this occurs at $t = 0.909$.

6 APPLICATION TO A PULSATING WHITE DWARF

6.1 Hydrostatic equilibrium

The problem of choosing an equilibrium fluid configuration is made non-trivial by the finite differencing of the dynamical equations. Consequently, a method to produce a solution for finite difference equations is required. For a barotropic equation of state, we have chosen to make use of the self-consistent field (SCF) method (see e.g. Motl et al. 2002; Hachisu 1986; Ostriker & Mark 1968). Because it is well described elsewhere, we will only summarize the procedure here.

(i) An initial guess for the density (taken from the continuum solution) is used to generate the gravitational potential via the method described in Section 4.

(ii) The new gravitational potential and the initial density guess are then used to calculate the Bernoulli constant at the centre of the star.

(iii) the Bernoulli constant and the new gravitational potential are used to calculate the enthalpy at all points on the grid, which is then subsequently inverted to yield the new density guess.

This procedure is iterated until the Bernoulli constant converges, that is, when the fractional change is less than some value, taken here to 10^{-15}. The resulting density distribution is a solution to

$$\frac{h_{+i} - h_{-i}}{2\Delta x^i} + \frac{\Phi_{+i} - \Phi_{-i}}{2\Delta x^i} = 0, \tag{35}$$

and hence no momentum flux is generated if the source terms are given by equation (19). Note that if the source terms are given by equation (18) this *will* produce a net momentum flux, and hence this is not necessarily a good approximation to equilibrium in that case.

When

$$\frac{\partial P}{\partial x^i} > \frac{P}{\Delta x^i}, \tag{36}$$

the pressure gradient required to preserve hydrostatic equilibrium cannot be resolved on the grid. For a star, this can result in strong, inwardly directed forces at the surface, driving shocks into the interior. We have found that adding an isothermal envelope can mitigate this problem by pushing the region where this inequality is true off of the grid, while adding an insignificant amount of mass to the star itself. This is done explicitly by setting a fiducial density (chosen here to be 10^{-2} of the central density) at which the equation of state changes from that of the cold white dwarf to a $\Gamma = 1$ polytrope. The polytropic constant is chosen such that $P(\rho)$ remains continuous across the transition. Table 1 compares the properties of the cold white dwarf with (HWD) and without (CWD) the isothermal envelope. Note that while the isothermal envelope increases the radius significantly, it does not change the mass or the frequency of the quadrupolar fundamental mode ($\omega_{\rm f2}$). The reason for this can be seen in Fig. 6. The f2 mode is more strongly weighted in the core where the addition of the isothermal envelope makes no difference. In contrast, the lowest order quadrupolar p mode ($\omega_{\rm p2}$) is substantially affected by the presence of the envelope. This is most likely results from the fact that the radial wavelength of the

Table 1. Stellar properties for a cold white dwarf with (CWD) and without (HWD) an isothermal envelope. Specifically, the mass, radius, fiducial stellar frequency $\omega_* = \sqrt{GM/R^3}$, frequency of the adiabatic $\omega_{\rm f2}$ mode, and the frequency of the lowest order adiabatic $\omega_{\rm p2}$ mode. Note that the inclusion of the isothermal envelope does not change the mass appreciably while significantly increasing the radius.

Model	$M(\mathrm{M}_\odot)$	$R(10^6$ m)	ω_*(Hz)	$\omega_{\rm f2}$(Hz)	$\omega_{\rm p2}$(Hz)
CWD	0.632	8.56	0.365	0.562	1.15
HWD	0.632	11.2	0.243	0.560	0.749

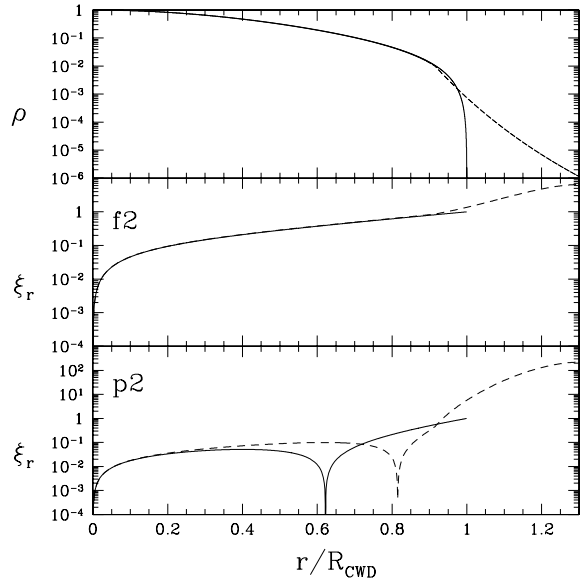

Figure 6. Shown in the top panel are the density profiles for the cold white dwarf with (solid) and without (dashed) the isothermal envelope. The two lower panels are the radial displacement profiles for the f2 mode and the lowest order p2 for the two models. Note that the density and f2-mode profiles are very nearly the same for the two cases. However, the mode profiles differ substantially for the p2 mode.

p2 is much closer to the height of the isothermal envelope. Henceforth, all evolutions were begun with the HWD model listed in Table 1.

The quality of the equilibrium generated by the SCF method may be explicitly demonstrated. Fig. 7 shows the evolution of the centre-of-mass position, net momentum and the fraction of the total energy that is converted into kinetic energy for a star initially in hydrostatic equilibrium. The last quantity is given in terms of the kinetic, internal and gravitational components:

$$K = \int \frac{1}{2}\rho v^2 d^3x, \quad \pi = \int p d^3x, \quad W = \int \rho\Psi d^3x. \tag{37}$$

Despite an initial exponential rise these quantities saturate at relatively low levels for all resolutions shown. Note that all times are measured in dynamical times of the cold white dwarf, $t_{\rm CWD} \equiv 1/\omega_*$, which is approximately the time it takes for a disturbance to cross the star. In particular, as seen in Table 1, the period of the f2 mode is about $4\pi t_{\rm CWD}/3$.

6.2 Oscillation modes

In general the problem of interest is dynamical. Specifically, we are interested in the non-linear evolution of the oscillation modes

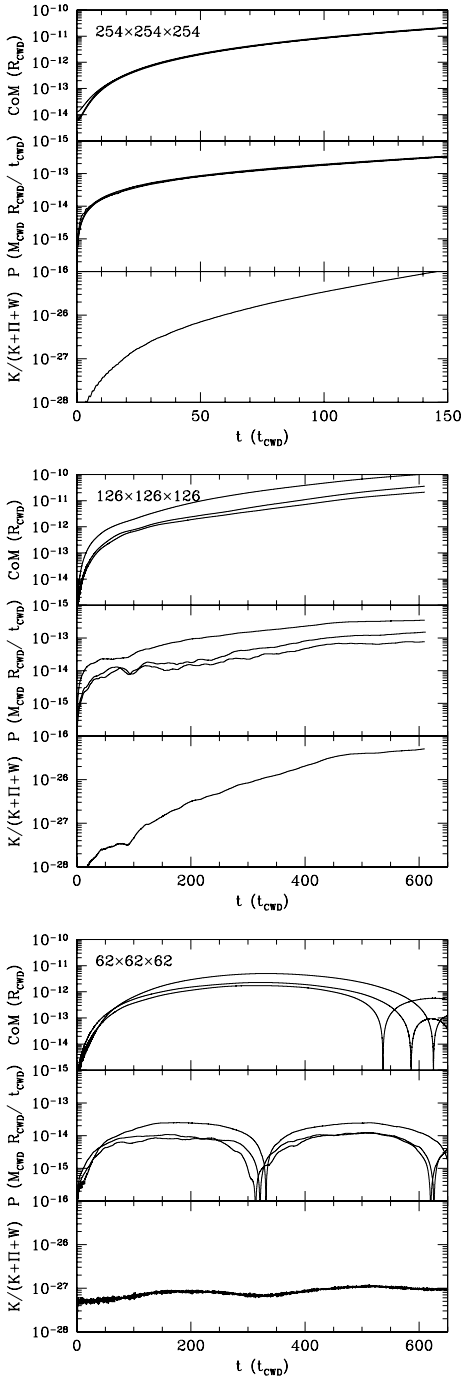

Figure 7. Shown are the centre-of-mass (top panels), net momentum (middle panels), and fraction of the total energy converted into kinetic energy (bottom panels) for a number of grid resolutions (note the different timescales). In all cases these quantities saturate well below significant levels (e.g. for the worst case, the centre-of-mass moves by less than 10^{-8} cell widths in the 150 dynamical times shown, thus it would require roughly 10^{13} dynamical times before the centre-of-mass moves one stellar radius. Typically, these appear to turn over implying that they may never rise significantly above 10^{-7} cell widths.)

of the cold white dwarf while undergoing resonant tidal excitation. Towards this end it is necessary to obtain a measure of the numerical quality factor (the e-folding time of the energy in the oscillation) and the oscillation frequencies themselves. That the latter may be

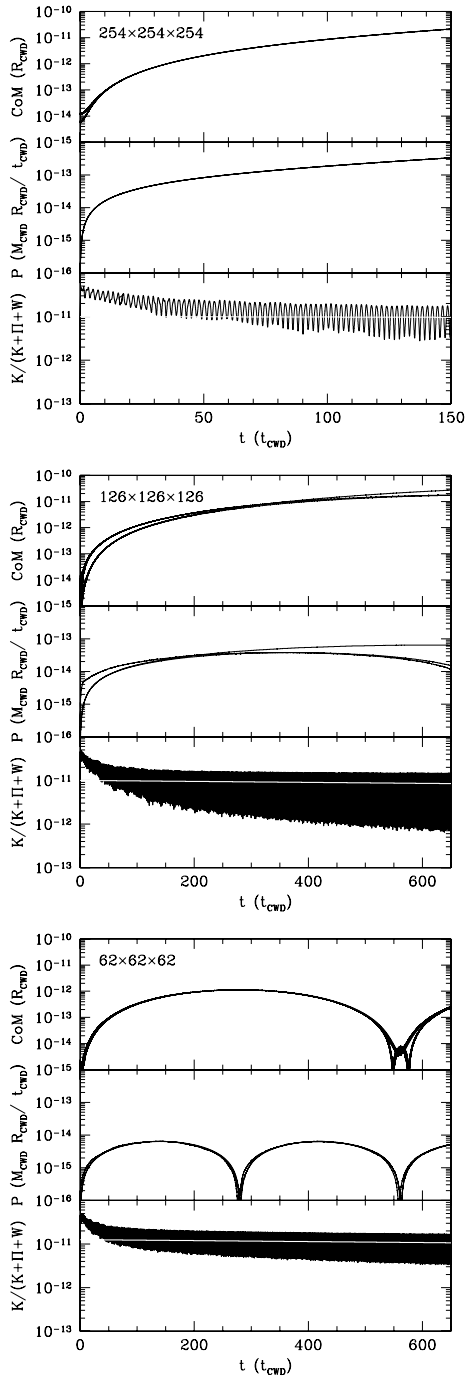

Figure 8. Same as Fig. 7 for the case when a quadrupolar perturbation is present (note the difference in scales in comparison to that figure). The white line drawn through the oscillations is for a Q of approximately 6000.

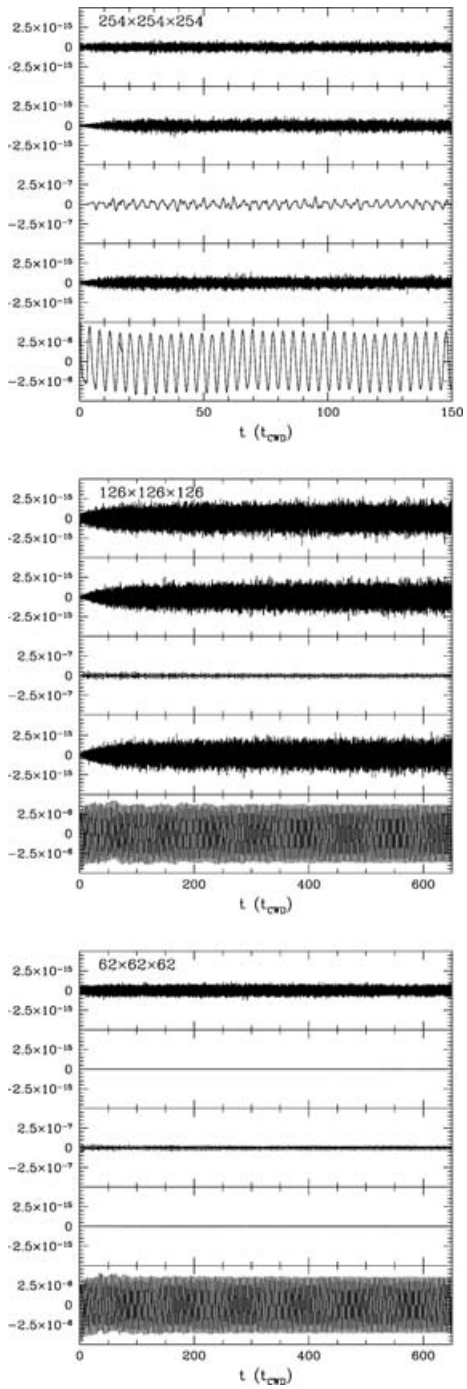

Figure 9. The quadrupolar moments of the perturbed star for each of the resolutions considered in Fig. 8. From top to bottom, the panels are the odd $m = 2$, odd $m = 1, m = 0$, even $m = 1$ and even $m = 2$ moments. Note the difference in scales of the different moments, namely that the even $m = 2$ moment is two orders of magnitude larger than the $m = 0$ moment (which is sourced by the Cartesian geometry) and nine orders of magnitudes larger than the others.

different from the frequencies in Table 1 is a result of both the approximation of discrete cells *and* the fact that the finite difference equations are distinct from the continuum equations used to generate the tabulated values. Both of these can be obtained by deforming the star in a particular way and analysing the subsequent oscillations.

We deformed the star by adding a fractional quadrupolar perturbation to the density, i.e.

$$\Delta\rho(\boldsymbol{r}) = A\rho(r)Y^e_{22}(\theta, \phi), \tag{38}$$

where the amplitude, A, was chosen to be small (10^{-4}) so that the resulting oscillation occurred in the linear regime. This will initiated an even $m = 2$ standing wave on the star. Figs 8 and 9 show the resulting evolutions for a number of grid resolutions. The same diagnostics as those used to demonstrate hydrostatic equilibrium are shown in Fig. 7. In this case as well, the centre-of-mass and

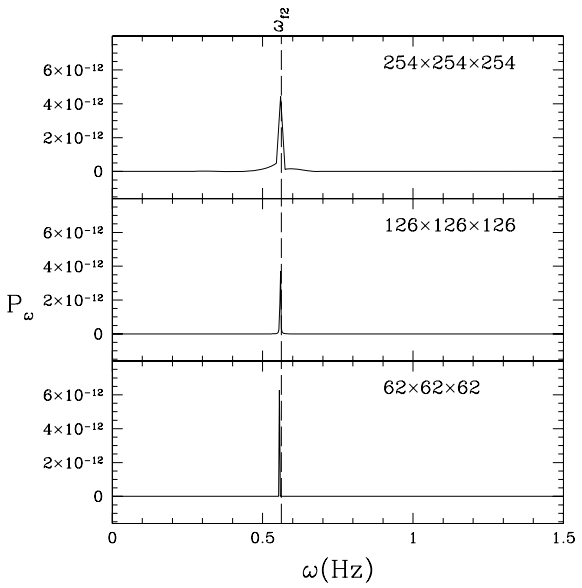

Figure 10. Shown are the power spectra of the even $m = 2$ quadrupolar moment as a function of angular frequency (using the mean squared amplitude normalization). As expected, for each grid resolution there is a strong spike coincident with the f2-mode frequency predicted for the HWD model.

momentum drift saturate at levels well below those of interest. Unlike hydrostatic equilibrium there now exists a non-vanishing kinetic energy. It is strongly harmonic and decays exponentially. Because the initial perturbation excited all of the even quadrupolar modes with $m = 2$, there are a number of distinct decay constants, with the slowest being due to the f2 mode. This exponential decay at late times may be fit to estimate the numerical Q, found here to be on the order of 6000.

In Fig. 9 the quadrupolar moments are shown. The even $m = 2$ moment is strongly dominant as expected. It also has a very clear harmonic structure. This may be Fourier analysed to produce the dominant oscillation mode, as shown in Fig. 10. In the periodogram of the even $m = 2$ quadrupolar moment is a peak which extends five orders of magnitude above the rest of the spectrum. This peak is clearly identifiable with the f2 mode and appears to have very nearly the frequency predicted by the HWD model.

7 CONCLUSIONS

We have developed and tested a parallel, simple and fast hydrodynamics code for multidimensional, self-gravitating, adiabatic flows. Both the advection terms and the solution for the self-gravity was greatly simplified by the use of a uniform Cartesian geometry, ultimately leading to explicit conservation of mass, entropy and momentum to machine accuracy. The simplifying assumption of adiabaticity and the absence of shocks eliminated the necessity for more numerically expensive schemes, yielding a fast code.

We have also applied our code to a number of standard diagnostic problems in order to verify its physical correctness and limitations. This was done in a systematic fashion intended to test each aspect of the code separately, including the advection scheme, the pressure source terms and finally the gravitational potential. Finally, we demonstrated the fitness of the code for the problem which motivated its development, the study of tidally excited adiabatic oscillations on WDs. This was done in two stages: first, verifying the long-term numerical stability of a WD in hydrostatic equilibrium, and secondly, measuring the numerical quality factor (found to be on the order of 6000) and the f2-mode frequency (found to be very nearly that predicted by a linear mode analysis of the HWD model). The details of tidally exciting adiabatic oscillations on WDs to non-linear amplitudes, and their subsequent evolution will be discussed in future publications.

ACKNOWLEDGMENTS

The authors would like to thank Anatoly Spitkovsky, Ruben Krasnopolsky, Michele Vallisneri, Andrew MacFadyen, Joel Tohline and Michael Norman for a number of helpful conversations. AEB would especially like to thank Jim Stone for a number of useful suggestions regarding the presentation of this material. This research used resources of the National Center for Computational Sciences at Oak Ridge National Laboratory, which is supported by the Office of Science of the US Department of Energy under Contract No. DE-AC05-00OR22725. This work was supported under NASA grant NAGWS-2837.

REFERENCES

Colbert E. J. M., Ptak A. F., 2002, ApJS, 143, 25
Colella P., Woodward P. R., 1984, J. Comp. Phys., 54, 174
Fryxell B. et al., 2000, ApJS, 131, 273
Gerssen J., van der Marel R. P., Gebhardt K., Guhathakurta P., Peterson R. C., Pryor C., 2002, AJ, 124, 3270
Hachisu I., 1986, ApJS, 62, 461
Hawley J. F., Wilson J. R., Smarr L. L., 1984, ApJ, 277, 296
Madau P., Rees M. J., 2001, ApJ, 551, L27
Motl P. M., Tohline J. E., Frank J., 2002, ApJS, 138, 121
Ostriker J. P., Mark J. W.-K., 1968, ApJ, 151, 1075
Press W. H., Teukolsky S. A., Vetterling W. T., Flannery B. P., 1992, Numerical Recipes in C, The Art of Scientific Computing, 2nd edn. Cambridge Univ. Press, Cambridge
Rathore Y., Broderick A. E., Blandford R., 2003, MNRAS, 339, 25
Rathore Y., Blandford R. D., Broderick A. E., 2005, MNRAS, 357, 834
Sod G. A., 1978, J. Comp. Phys., 27, 1
Stone J. M., Norman M. L., 1992, ApJS, 80, 753
van Leer B., 1977a, J. Comp. Phys., 23, 263
van Leer B., 1977b, J. Comp. Phys., 23, 276
van Leer B., 1979, J. Comp. Phys., 32, 101

This paper has been typeset from a TEX/LATEX file prepared by the author.